Electroluminescence hyperspectral imaging of light-emitting diodes using a liquid crystal tunable filter

Paul R. Edwards,[a] (iD) Jochen Bruckbauer, (iD) Douglas Cameron, (iD) and Robert W. Martin (iD)

AFFILIATIONS

Department of Physics, SUPA, University of Strathclyde, 107 Rottenrow, Glasgow G4 0NG, United Kingdom

[a]Author to whom correspondence should be addressed: paul.edwards@strath.ac.uk

ABSTRACT

We demonstrate the use of a low-cost liquid-crystal-based wavelength-tunable filter and CMOS video camera to add hyperspectral imaging capabilities to a probe station equipped with a simple optical microscope. The resultant setup is used to rapidly resolve the spectral and spatial variations in electroluminescence typically observed for $In_xGa_{1-x}N/GaN$ light-emitting diodes. Applying standard statistical analyses of variation within the multivariate datasets, such as moments and principal components, we observe inhomogeneities on a spectral scale significantly smaller than the bandwidth of the tunable filter. The resultant tool offers an alternative to scanning beam luminescence techniques for high-throughput hyperspectral analysis of optoelectronic devices.

Spectroscopic analysis of the light emitted from semiconductors is an essential characterization tool both for investigating the band structure of constituent materials and for evaluating the performance of full optoelectronic devices such as light-emitting diodes (LEDs). This analysis is routinely carried out by exciting emission using beams of photons (photoluminescence: PL) or electrons (cathodoluminescence: CL)[1] or by direct injection of an electric current (electroluminescence: EL). In addition to spectroscopic analysis of this luminescence, spatial information can be obtained by acquiring wavelength-filtered images of the component peak intensities.

For some materials such as the technologically important alloys of the group-III nitrides ($In_xGa_{1-x}N$, $Al_xGa_{1-x}N$, etc.), their inherent spatial inhomogeneity makes it desirable to measure them in the *hyperspectral imaging* (HSI) mode.[2] Variations in alloying, doping, elastic strain, and temperature are just a few of the factors, which can cause subtle spectral shifts with position, and only a combined spatial/spectral dataset (or *data-cube*) can fully capture this behavior.

The experimental setups required for PL/CL experiments do not lend themselves to the "push-broom" (i.e., one complete spatial line at a time) method of HSI acquisition, the most widely favored approach in remote sensing, flat-bed scanning, and other reflected light applications. Instead, the fact that the spatial resolution of beam-based luminescence measurements is determined by the spot size of the exciting

beam—while the rest of the sample area remains dark—means that the natural sequence of data acquisition is one spatial pixel (i.e., one spectrum) at a time. This method of building up the data cube is slow but in microscopic applications remains the only way of ensuring that the spatial resolution of the HSI is not limited by far-field diffraction in the collection optics.

For equivalent electroluminescence (ELHSI) measurements, however, the requirements change. EL is emitted from an extended area; this loss of spatial selectivity in the excitation means that we must instead achieve spatial resolution using the collecting optics. Confocal geometry is one option with a pinhole in the collection path limiting the spectral analysis to that light coming from a small area of a scanning sample.[3,4] However, this imposes similar speed restrictions to those of scanning PL/CL measurements, without the associated resolution benefits, and wastes most of the emitted light. Spectral mapping using scanning near-field optical microscopy (SNOM) overcomes the resolution limit[5] but is equally slow. None of these approaches offers the high-throughput device evaluation that is desirable in a laboratory and essential for industrial in-line quality control.

More efficient methods of acquiring an ELHSI dataset use a 2D sensor array. This can involve spectrally dispersing the light in one dimension while imaging in the other and resolving in the second spatial dimension by scanning the sample; this push-broom geometry is

routinely used in non-microscopic EL applications.[6] Alternatively, an optical microscope can be employed to directly image the full device to the sensor and apply bandpass spectral filtering to achieve wavelength selectivity; stepping the filter wavelength then builds up a hyperspectral image one monochromatic frame at a time. Multiple fixed-wavelength interference bandpass filters can be used,[7] but this is slow due to the need to mechanically switch between filters, and the spectral resolution is limited by the filter bandwidth and the number of filters employed. An improvement on this approach is to instead use a tunable bandpass filter, and this has been successfully implemented using Bragg grating filters (e.g., for measuring EL from solar cells).[8] Such setups are expensive, due, in part, to the requirement for precision customized optics for line scanning.

In this work, we describe a setup which instead uses a liquid-crystal-based tunable bandpass filter and use it to characterize an $In_xGa_{1-x}N$/GaN light-emitting diode (LED) and μLED array. Such filters have a clear aperture through which imaging can be carried out using standard optical lenses. This type of filter has previously been used extensively in non-EL hyperspectral applications.[9,10] Here, we focus particularly on the effectiveness of this approach for *spectral* analysis, in which we extract maps of spectral parameters other than just intensities, such as peak wavelengths and widths. This is a particular requirement for analyzing semiconductor luminescence and is distinct from that encountered in more general hyperspectral imaging applications, where the challenge is usually that of unmixing combinations of spectral end-members.[11]

The HSI optics considered here could, in principle, be attached to any macro- or microscopic luminescence setup, but here we demonstrate their use on a custom-built probe station. This setup allows the contacting of unbonded LED dies and includes an integrated stereo zoom microscope (BSR model, Brunel Microscopes Ltd.) with a trinocular output port. The system projects an image to a focal plane approximately 11 mm beyond the output flange without requiring additional optics. This leaves room for a tunable filter to be inserted before an imaging camera with a ray convergence angle within the acceptance angle of the filter (in this case 6°). Figure 1 shows a schematic outline of the setup; note that the optical components are not shown to scale with the effect that the convergence angle of the rays through the tunable filter is exaggerated.

The tunable filter (Kurios-VB1, Thorlabs, Inc.) is a liquid crystal-based device with a 20 mm diameter clear aperture. It is tunable in 1 nm steps within the range 420–730 nm, and we use its narrow (nominally 10 nm) bandwidth setting. Both the peak transmittance and the bandwidth vary with the center wavelength, and we use manufacturer-provided functions to correct the spectral intensity of the measured data. The particularly strong correction applied at the blue end of the spectrum necessitates accurate subtraction of any background (due to detector dark counts or offset in the analog-to-digital converter) to avoid the appearance of short-wavelength spectral artifacts.

An 8.9-megapixel passively cooled monochrome CMOS camera (Kiralux CS895MU, Thorlabs, Inc.) is connected directly to the tunable filter, and the position of this assembly is tuned so that the camera focus coincides with the focus observed through the microscope's binocular eyepieces; these can then be used for focusing of subsequent samples. The spectral response of the camera is corrected for using tabulated wavelength-dependent quantum efficiency values provided by the manufacturer.
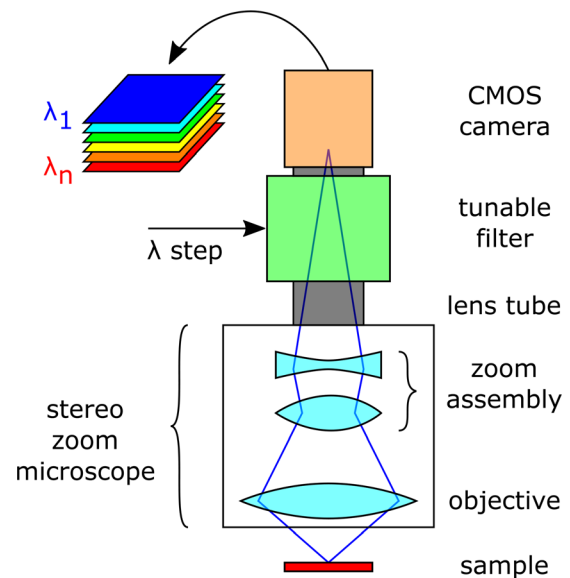

FIG. 1. Schematic diagram of the microscope with HSI optics added (not drawn to scale).

We adjust the camera gain and exposure time such that the peak intensity falls just below the 12-bit saturation point of its analog-to-digital converter, maximizing the measurement's dynamic range. The exposure time is then kept constant, and successive frames are acquired as the wavelength is scanned through the full 420–730 nm range in 1 nm increments (i.e., 311 monochromatic frames, each corresponding to one spectral channel). Total acquisition time is dependent on the sample brightness and is on the order of a few tens of seconds. This is approximately two orders of magnitude faster than a comparable CLHSI due to the parallel acquisition of 2D spatial images compared with the parallel acquisition of 1D spectra in scanning beam techniques. The resultant stack of aligned monochromatic images is up to $\approx$1.3 GB in size (without binning, cropping, or compression); this is imported into in-house HSI software for spectral response correction and further analysis.

For a first demonstration of the system, we measured an unpackaged 1 mm^2 blue InGaN/GaN light-emitting diode (LED), fabricated using GaN-on-silicon technology. Figure 2 shows the area-averaged spectrum extracted from an EL hyperspectral image acquired from the device. The emission is dominated by a quantum well (QW) emission peak at 2.75 eV with unresolved shoulders on its low energy side. This asymmetry—which could be due to longitudinal optical phonon replicas ($\Delta E \approx 90$ meV in InGaN QWs),[12] or differences between the emission energies of the multiple QWs—makes it difficult to fit the peak to a simple function such as a Gaussian.

However, spatial inhomogeneities in an emission peak can also be visualized by extracting maps from the hyperspectral image related to statistical *moments* of the spectrum.[1] Figures 3(a)–3(c) show examples calculated over the 2.4–2.9 eV spectral range (marked as a shaded box in Fig. 2). The zeroth moment [Fig. 3(a)] represents an integration of the intensity over the given range (i.e., a bandpass-filtered image). The first moment [Fig. 3(b)] is a center of mass, or "centroid," which allows energy shifts to be seen. The second moment is the variance,
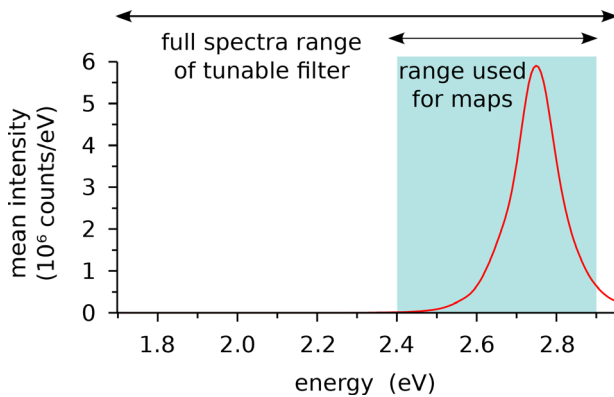
18 September 2023 08:03:25

FIG. 2. Mean spectrum extracted from the ELHSI of a blue LED. The 2.4–2.9 eV spectral range used to calculate the maps in Fig. 3 is marked.

highlighting changes in the peak width; here, we plot the square root of this [i.e., the standard deviation or—equivalently—root mean square, Fig. 3(c)] so that peak width variations can be viewed in units of energy.

These results reveal spatial inhomogeneity in the intensity, position, and width of the QW peak. Combined spectral/spatial features of this nature are commonly seen in such devices grown on mismatched substrates and stem from the induced strain fields and their effect on alloy composition or from topography on the GaN-on-silicon substrates. We can clearly distinguish spectral shifts and peak width variations on the order of a millielectronvolt, significantly smaller than the bandwidth of the tunable filter ($\approx$38 meV at 2.74 eV).

We previously demonstrated the use of principal component analysis (PCA) as a semi-automated method of identifying the dominant spectral components of a CL hyperspectral image,[1,13] and we apply this now to the EL dataset. This method re-orders the data, so that instead of the HSI being described by the sum of the 311 originally acquired monochromatic frames, it can now be described (equivalently and without loss) by the sum of 311 new images each associated with an orthogonal (but non-monochromatic) spectrum; importantly, these components are now ordered by their contribution to the total data variance, so that the most significant ones can now be retained and the less-significant (noise-dominated) components discarded. The remaining *principal components*, each of unit intensity, therefore, represent a new set of basis vectors with which to describe the data.

Figure 4 shows the first three principal components of the same HSI that was used to generate the maps in Figs. 3(a)–3(c). The first component accounts for >99% of the variance in the dataset and is almost identical to the mean spectrum seen in Fig. 2. The next two components closely resemble the first and second derivative functions of the peak shape, respectively. This can be understood by considering the additive components required to construct a peak, which is varying in both spectral position and width. Adding to one side of the peak and subtracting from the other (as in the second component) has the effect of shifting the peak energy, while adding to the tails and subtracting from the peak (or vice versa) will broaden (or narrow) the peak (third component). This interpretation is confirmed by the inspection of the maps (or, in PCA nomenclature, the *scores*), which show the contribution of each component at each spatial pixel [Figs. 3(d)–3(f)], which very closely follow the maps of the moments in Figs. 3(a)–3(c).
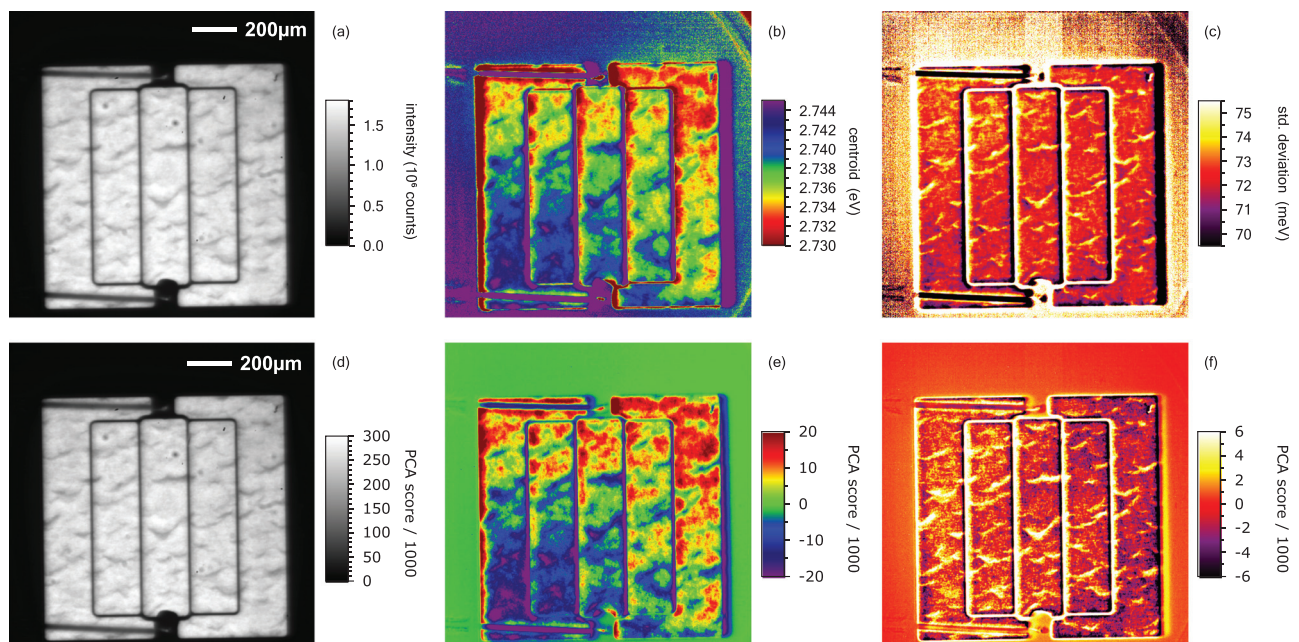

FIG. 3. Maps extracted from a single EL hyperspectral image of a blue LED. (Top) Statistical moments calculated over the spectral range 2.4–2.9 eV: (a) integrated intensity (0th moment); (b) centroid (1st moment); (c) standard deviation ($\sqrt{\text{2nd moment}}$). (Bottom) Maps of the scores of the first three principal components, with (d)–(f) corresponding to the 1st, 2nd, and 3rd spectra seen in Fig. 4, respectively.
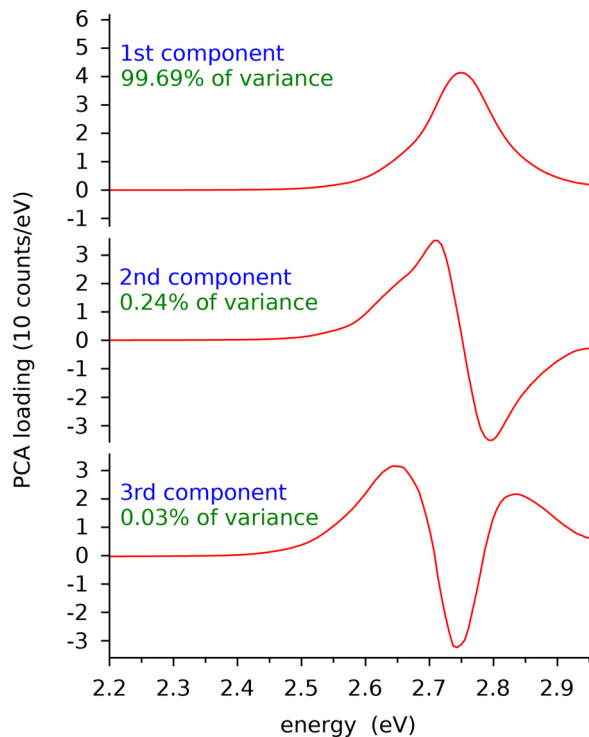
FIG. 4. First three principal components (loadings) of the blue LED HSI dataset.

We note here that any additional spectral peaks which did not perfectly co-vary with the observed peak would be identified by the PCA as an additional principal component. Conversely, any spectral features whose intensity varied proportionally with another peak would be interpreted in the analysis as part of the same component; in this way, for example, it is possible to readily identify a second-order peak in spectrometer-based measurements, where this peak intensity closely tracks that of the first-order peak. While our tunable filter approach avoids such higher-order diffraction effects, comparable artifacts may also occur through the leaking of light through the filter at certain wavelengths due to imperfect stop-bands in the transmission spectrum.

As a second example, we measured an array of yellow/green μLEDs using the same ELHSI setup. This device had been fabricated by dry-etching pillars into planar LED wafer material, before being bonded to a CMOS driver array in a flip-chip configuration to produce an addressable μLED array.[14,15] Figure 5 shows the area-averaged spectrum, again dominated by a single QW band. Maps of the moments (Fig. 6) again show the sensitivity of the technique to be comfortably capable of revealing spatial and spectral inhomogeneities associated with such devices, despite the limited spectral bandwidth of the tunable filter. Immediately noticeable in the intensity map is the higher brightness at the peripheries of the micropillars, which we have attributed to the enhancement of light extraction through scattering from the sidewalls.[16] The data also reveal more pronounced and asymmetric darkening near the center of many of the pillars, indicating that damage has occurred to the p-layer of the diode during fabrication due to an insufficiently optimized bump-bonding process used for

attaching the CMOS driver array. This interpretation of device damage is confirmed by the peak broadening seen in the corresponding pixels of the standard deviation map.

This use of a wide-field technique and a camera lets us acquire many more spatial pixels compared with scanning techniques, without slowing the acquisition. This is demonstrated in Fig. 7, which shows maps from a 176 × 165-pixel cropped region from the 1200 × 1200-pixel dataset of Fig. 6. Because it is not possible to reliably extract peak positions and widths from a noise-dominated low-intensity peak, we have masked (in black) those pixels in the centroid and standard deviation maps corresponding to low intensities, leaving the variation in the remaining pixels to be more clearly seen. The high spatial definition allows us to examine small areas of an ELHSI without excessive pixelation; in this case, we note a spectral shift in the emission across a single μLED similar to that which we previously observed in comparable devices using a much slower CL mapping system.[17] In this case, a blue-shift in the emission peak near the periphery of the μLED has resulted from a local relaxation (due to the free surface) of the compressive strain, which is typically locked in to such devices.[18] This strain includes contributions from the lattice mismatch at each hetero-interface but is typically dominated by the mismatch in thermal expansion coefficient between the nitride layers and the substrate.[19] This strain relaxation has, in turn, lowered the piezoelectric field in the active layers, reducing the quantum-confined Stark effect and causing the QWs to emit at higher energies.[20]

In cases where multiple spectral features of interest are unresolved, neither the moments nor PCA approaches will be sufficient to spectrally separate the peaks. This could be the case, for example, with narrow peaks due to optical modes in Fabry–Pérot or whispering gallery cavities, or with the sharp spectral lines seen in the emission from rare-earth-doped materials. Future work will aim to demonstrate peak deconvolution with spectral resolution better than the bandwidth of the tunable filter; in principle, some improvement may be gained by exploiting spectral oversampling (e.g., shifting a 10 nm wide stop band in 1 nm steps) and rigorous characterization of the transmission filter response. While the spectral resolution will not compete with that attainable using grating-based spectrometers, the resolution already demonstrated will be sufficient for a wide range of devices such as LEDs and solar cells whose EL is characterized by broad emission bands. Tunable filters with different spectral ranges may be required for some applications; e.g., near-infrared designs are commercially
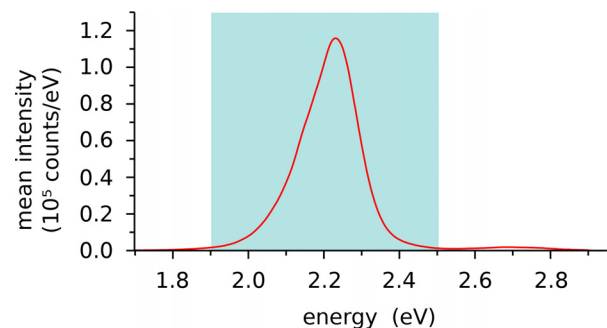

FIG. 5. Mean spectrum extracted from an ELHSI of a yellow/green μLED array. The 1.9–2.5 eV spectral range used to calculate the maps in Figs. 6 and 7 is marked.
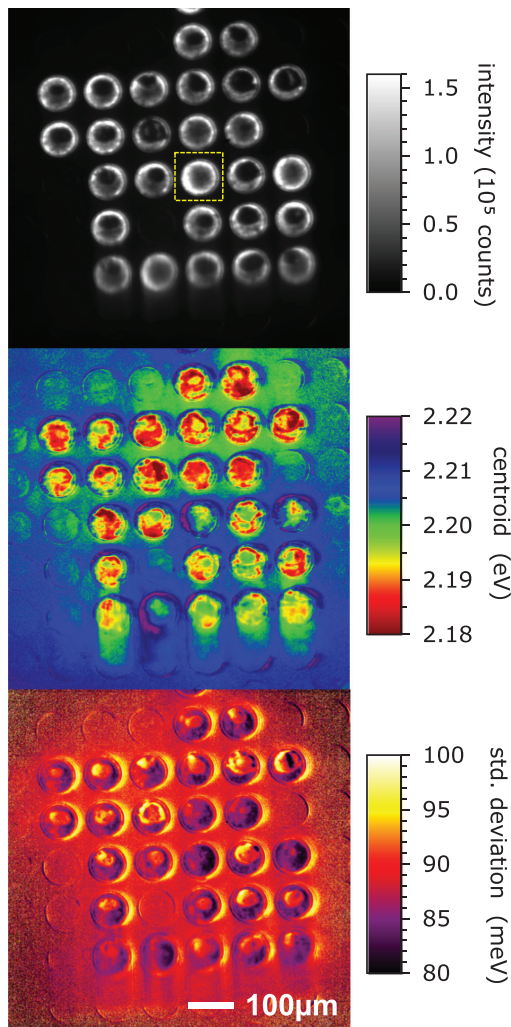
FIG. 6. Maps extracted from the EL hyperspectral image of a yellow/green μLED array, showing the first three statistical moments calculated over the 1.9–2.5 eV spectral range, which correspond to the emission intensity, peak position, and width.

FIG. 7. Detailed area of a single μLED, cropped from the region marked in Fig. 6. To improve clarity, noise-dominated regions outside the pillar have been masked in the centroid and standard deviation maps using an intensity threshold.

available, which could be used for narrow-bandgap applications such as solar cells.

The tunable filter is of a Lyot design[21] based on a birefringent crystal and, hence, transmits only one linearly polarized component of the incident light. This will have little effect on the example data presented here, whose active layers are ⟨0001⟩-oriented wurtzite GaN and, thus, in-plane isotropic, apart from a loss of 50% in the light intensity. For measurements on samples with polarized emission (e.g., semi- and non-polar nitride QWs), the polarized detector response will need to be considered and may potentially be exploited. This will be of particular importance in the measurement of high-AlN-content $Al_xGa_{1-x}N$ alloys,[22,23] although the lack of tunable filters operating in the ultraviolet range would first need to be addressed.

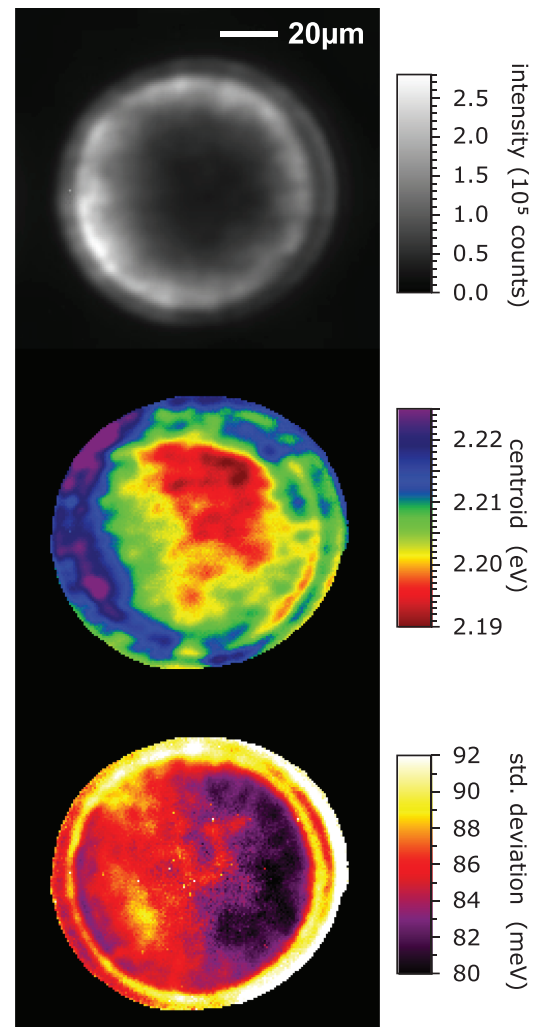We have shown that the spectral and spatial inhomogeneity of GaN-based LEDs can be rapidly assessed through the use of a low-cost hyperspectral imaging upgrade to an optical microscope, employing a liquid-crystal tunable filter. When characterizing samples whose emission is dominated by a single peak, this approach has been shown to be capable of mapping variations in the peak position and width, which are considerably smaller than the filter bandpass FWHM. These subtle variations have been analyzed by techniques (moments and principal components), which exploit the statistical wealth of information in an HSI with the results of these approaches shown to be in close agreement. This approach allows us to quickly and cheaply characterize the micro-scale spectral variations, which are essential to the performance of optoelectronic devices.

18 September 2023 08:03:25

AUTHOR DECLARATIONS
Conflict of Interest

Author Contributions

Paul R. Edwards: Conceptualization (equal); Data curation (equal); Funding acquisition (supporting); Investigation (equal); Methodology (equal); Software (lead); Writing – original draft (lead); Writing – review & editing (equal). **Jochen Bruckbauer:** Conceptualization (equal); Data curation (equal); Investigation (equal); Methodology (equal); Writing – review & editing (equal). **Douglas Cameron:** Investigation (equal); Methodology (equal); Writing – review & editing (equal). **Robert W. Martin:** Conceptualization (equal); Data curation (equal); Funding acquisition (lead); Investigation (equal); Methodology (equal); Project administration (lead); Supervision (lead); Writing – review & editing (equal).

DATA AVAILABILITY

The data that support the findings of this study are openly available in the University of Strathclyde KnowledgeBase at https://doi.org/10.15129/1d98de3e-6e96–418e-a782–4bfe464dd748, Ref. 24.

REFERENCES

[1]P. R. Edwards, L. K. Jagadamma, J. Bruckbauer, C. Liu, P. Shields, D. Allsopp, T. Wang, and R. W. Martin, "High-resolution cathodoluminescence hyperspectral imaging of nitride nanostructures," Microsc. Microanal. **18**, 1212 (2012).

[2]R. W. Martin, P. R. Edwards, K. P. O'Donnell, M. D. Dawson, C. W. Jeon, C. Liu, G. R. Rice, and I. M. Watson, "Cathodoluminescence spectral mapping of III-nitride structures," Phys. Status Solidi A **201**, 665 (2004).

[3]P. Fischer, J. Christen, and S. Nakamura, "Spectral electroluminescence mapping of a blue InGaN single quantum well light-emitting diode," Jpn. J. Appl. Phys. **39**, L129 (2000).

[4]M. J. Wallace, P. R. Edwards, M. J. Kappers, M. A. Hopkins, F. Oehler, S. Sivaraya, R. A. Oliver, C. J. Humphreys, D. W. E. Allsopp, and R. W. Martin, "Effect of the barrier growth mode on the luminescence and conductivity micron scale uniformity of InGaN light emitting diodes," J. Appl. Phys. **117**, 115705 (2015).

[5]G. Marutsuki, Y. Narukawa, T. Mitani, T. Mukai, G. Shinomiya, A. Kaneta, Y. Kawakami, and S. Fujita, "Electroluminescence mapping of InGaN-based LEDs by SNOM," Phys. Status Solidi A **192**, 110 (2002).

[6]M. P. Peloso, J. Sern Lew, T. Trupke, M. Peters, R. Utama, and A. G. Aberle, "Evaluating the electrical properties of silicon wafer solar cells using hyperspectral imaging of luminescence," Appl. Phys. Lett. **99**, 221915 (2011).

[7]A. Giles, J. Caldwell, R. E. Stahlbush, B. A. Hull, N. Mahadik, O. Glembocki, K. Hobart, and K. X. Liu, "Electroluminescence spectral imaging of extended defects in 4H-SiC," J. Electron. Mater. **39**, 777 (2010).

[8]S. M. Chavali, J. Roller, M. Dagenais, and B. H. Hamadani, "A comparative study of subcell optoelectronic properties and energy losses in multijunction solar cells," Sol. Energy Mater. Sol. Cells **236**, 111543 (2022).

[9]N. Gat, "Imaging spectroscopy using tunable filters: A review," *Wavelet Applications VII*, edited by H. H. Szu, M. Vetterli, W. J. Campbell, and J. R. Buss (SPIE, 2000), Vol. 4056, p. 50.

[10]R. W. Slawson, Z. Ninkov, and E. P. Horch, "Hyperspectral imaging: Wide–area spectrophotometry using a liquid–crystal tunable filter," Publ. Astronomical Soc. Pacific **111**, 621 (1999).

[11]J. M. Bioucas-Dias, A. Plaza, N. Dobigeon, M. Parente, Q. Du, P. Gader, and J. Chanussot, "Hyperspectral unmixing overview: Geometrical, statistical, and sparse regression-based approaches," IEEE J. Sel. Top. Appl. Earth Observations Remote Sens. **5**, 354 (2012).

[12]R. Pecharromán-Gallego, P. R. Edwards, R. W. Martin, and I. M. Watson, "Investigations of phonon sidebands in InGaN/GaN multi-quantum well luminescence," Mater. Sci. Eng. B **93**, 94 (2002).

[13]P. R. Edwards, R. W. Martin, and M. R. Lee, "Combined cathodoluminescence hyperspectral imaging and wavelength dispersive X-ray analysis of minerals," Am. Miner. **92**, 235 (2007).

[14]Z. Gong, N. Y. Liu, Y. B. Tao, D. Massoubre, E. Y. Xie, X. D. Hu, Z. Z. Chen, G. Y. Zhang, Y. B. Pan, M. S. Hao, I. M. Watson, E. Gu, and M. D. Dawson, "Electrical, spectral and optical performance of yellow–green and amber micro-pixelated InGaN light-emitting diodes," Semicond. Sci. Technol. **27**, 015003 (2012).

[15]S. Zhang, Z. Gong, J. J. D. McKendry, S. Watson, A. Cogman, E. Xie, P. Tian, E. Gu, Z. Chen, G. Zhang, A. Kelly, R. K. Henderson, and M. D. Dawson, "CMOS-controlled color-tunable smart display," IEEE Photonics J. **4**, 1639 (2012).

[16]H. W. Choi, C. W. Jeon, M. D. Dawson, P. R. Edwards, R. W. Martin, and S. Tripathy, "Mechanism of enhanced light output efficiency in InGaN-based microlight emitting diodes," J. Appl. Phys. **93**, 5978–5982 (2003).

[17]E. Y. Xie, Z. Z. Chen, P. R. Edwards, Z. Gong, N. Y. Liu, Y. B. Tao, Y. F. Zhang, Y. J. Chen, I. M. Watson, E. Gu, R. W. Martin, G. Y. Zhang, and M. D. Dawson, "Strain relaxation in InGaN/GaN micro-pillars evidenced by high resolution cathodoluminescence hyperspectral imaging," J. Appl. Phys. **112**, 013107 (2012).

[18]L. Dai, B. Zhang, J. Y. Lin, and H. X. Jiang, "Comparison of optical transitions in InGaN quantum well structures and microdisks," J. Appl. Phys. **89**, 4951–4954 (2001).

[19]S. Nakamura and G. Fasol, *The Blue Laser Diode: GaN Based Light Emitters and Lasers* (Springer, Berlin, 1997).

[20]T. Takeuchi, S. Sota, M. Katsuragawa, M. Komori, H. Takeuchi, H. Amano, and I. Akasaki, "Quantum-confined Stark effect due to piezoelectric fields in GaInN strained quantum wells," Jpn. J. Appl. Phys. **36**, L382 (1997).

[21]B. Lyot, "Un monochromateur à grand champ utilisant les interférences en lumière polarisée," C. Rend. l'Académie Sci. **197**, 1593 (1933).

[22]K. B. Nam, J. Li, M. L. Nakarmi, J. Y. Lin, and H. X. Jiang, "Unique optical properties of AlGaN alloys and related ultraviolet emitters," Appl. Phys. Lett. **84**, 5264 (2004).

[23]T. Kolbe, A. Knauer, C. Chua, Z. Yang, S. Einfeldt, P. Vogt, N. M. Johnson, M. Weyers, and M. Kneissl, "Optical polarization characteristics of ultraviolet (In)(Al)GaN multiple quantum well light emitting diodes," Appl. Phys. Lett. **97**, 171105 (2010).

[24]P. R. Edwards, J. Bruckbauer, D. Cameron, and R. W. Martin (2023). "Electroluminescence hyperspectral imaging of light-emitting diodes using a liquid crystal tunable filter," University of Strathclyde KnowledgeBase. https://doi.org/10.15129/1d98de3e-6e96-418e-a782-4bfe464dd748